Application of the NSCD method to analyse the dynamic behaviour of stone arched structures

Ali Rafiee, Marc Vinches, Claude Bohatier

To cite this version:

Ali Rafiee, Marc Vinches, Claude Bohatier. Application of the NSCD method to analyse the dynamic behaviour of stone arched structures. International Journal of Solids and Structures, 2008, 45 (25-26), pp.6269-6283. 10.1016/j.ijsolstr.2008.07.034 . hal-03260501

HAL Id: hal-03260501
https://imt-mines-ales.hal.science/hal-03260501v1

Submitted on 5 Jun 2023

Application of the NSCD method to analyse the dynamic behaviour of stone arched structures

Ali Rafiee [a,1], Marc Vinches [a,*], Claude Bohatier [b,2]

[a] *Alès School of Mines, 6 av. de Clavières, 30319 Alès cedex, France*
[b] *LMGC-UMR 5508, Université MONTPELLIER II, CC 048 Place Eugène Bataillon, 34095 Montpellier cedex 5, France*

ABSTRACT

In this paper, a masonry arch is simulated in order to assess both its structural and seismic vulnerability. The non-smooth contact dynamics (NSCD) computational method is used to simulate this type of structure as a collection of bodies under the hypothesis of unilateral constraints and frictional contact, with or without cohesion. Sinusoidal oscillations in three dimensions and real earthquake data have been applied to the supporting base element of the arch model.

The primary aim of this study is to better understand the dynamic behaviour of the masonry arch, a typical component of historic unreinforced masonry (URM) structures. This study also assesses the influences of the input parameters on the mechanical and dynamic behaviour of the arch structure. Its collapse mechanism is studied for both cohesive and non-cohesive contact.

In addition, we examine the behaviour under seismic loading of the Arles aqueduct, a real historical arched structure located in the south-east of France. Significant information can be obtained from the comparison of the results of advanced numerical analysis, taking into account the precise geometry of the model, the mechanical characteristics of the materials and the observation of the *in situ* monuments after their collapse.

Keywords:
NSCD method
Discrete model
Arched structure
Masonry
Earthquake

1. Introduction

Masonry arches are one of the most familiar structural shapes present in the worldwide architectural heritage. Historical domed buildings, arched stone bridges and vaulted tunnels are among the most common examples. The predictability of the behaviour of masonry arches is still the subject of mechanical research (Acary et al., 1999; Brookes and Mullett, 2004; DeJong et al., 2007; Drosopoulos et al., 2006; Drosopoulos et al., 2007; Drosopoulosa et al., 2006; Fanning and Boothby, 2001; Ford et al., 2003; Gilbert and Melbourne, 1994; Heyman, 1982; Hofstetter and Mang, 1995; Idris et al., 2007; Melbourne and Gilbert, 1995; Ng and Fairfield, 2004; Orduna and Lourenço, 2005; Orduna and Lourenço, 2005; Winkler et al., 1995).

Over the last few years, the development of numerical tools in the field of structural analysis has enabled researchers to establish approaches for the numerical modelling of masonry structures. However, an analysis of the mechanical behaviour of such blocks and joint structures remains challenging due to the influence of numerous factors.

The limitations of analytical modelling enhance the usefulness of numerical modelling for URM structures. Advances in non-linear finite element modelling have made it an increasingly more appropriate tool for the analysis of URM structures.

---

* Corresponding author. Tel.: +33 4 66 78 56 67; fax: +33 4 66 78 53 65.
E-mail addresses: ali.rafiee@ema.fr (A. Rafiee), marc.vinches@ema.fr (M. Vinches), bohatier@lmgc.univ-montp2.fr (C. Bohatier).

The application of the discrete element modelling inherently captures the discontinuous nature of the masonry and allows for a fully dynamic analysis with large displacements.

Several modelling approaches of masonry structures (continuous and discontinuous modelling) are currently under development by several research teams (Idris et al., 2007). A number of masonry arch models have been proposed in order to study their behaviour and some instability problems, Ford et al. (2003), Sumon and Ricketts (1995), Hughes and Davies (1998), Bicanic et al. (1995) and Brookes and Mullett (2004).

By considering all of these studies, three basic modelling strategies for masonry structures can be identified:

1– Continuous methods: the finite difference method (FDM), the finite element method (FEM), and the boundary element method (BEM).
2– Discrete methods: the discrete element method (DEM), and discrete fracture networks method (DFN).
3– Hybrid Continuous/Discrete methods (Jing, 2003).

In the present paper, our objective is to study the stability and collapse mechanisms of the masonry arch submitted to a sinusoidal motion, as a first step toward the simulation of an earthquake loading.

The masonry arch is modelled with the discrete element method using the open platform program LMGC90® (Dubois, 2003), which is based on the NSCD algorithm. This code allows us to model granular materials, made of rigid or deformable bodies, with complex mechanical behaviour (elasto-plastic, damaged materials) or interactions (frictional and cohesive contacts). LMGC90® (Dubois, 2003) is based on a hybrid or extended FEM–DEM discretization, using various numerical strategies, such as molecular dynamics MD or NSCD.

We will begin with a global presentation of the NSCD method, its main features and its advantages in comparison with other discrete elements methods. Then, we will present the modelling results of two three dimensional models having the same geometry but different conditions or parameters for the definition of the contact interactions. Finally, the results obtained from these two rigid models will be compared.

2. The NSCD method

2.1. Parametrization and equation of dynamics

In computational mechanics, among well-suited approaches for the rigid body dynamics with contact, friction and impact, there are two opposite approaches: compliant versus unilateral contact model and event-driven versus time-stepping schemes. In the context of granular materials, where large collections of bodies are encountered, Cundall (1979) was the first to propose a numerical tool, based on an Euler scheme, where contacts are governed by a compliant model. With a very different approach, Moreau (1998), Moreau (1988) and Jean (1999), Jean et al. (2001), Jean and Moreau (1992) exposed a numerical treatment of rigid and deformable body collections with unilateral contact, Coulomb's dry friction and impact, in the framework of the non-smooth mechanics and convex analysis. This framework yields a time-stepping scheme (without explicit event-handling) where velocities and impulses are the primary variables.

This section aims at representing the basic equations of the non-smooth contact dynamics method (NSCD). The formulation of the NSCD method relies on a special formulation of the equation of motion. The term "non-smooth" refers firstly to the mathematical and mechanical background allowing us to deal with some extended kinds of laws. For the non-smoothness in time, the occurrence of velocity jumps is a well-known feature of the second order dynamics with unilateral constraints on the position, even with continuous media.

Additionally, the contact forces between two bodies are bound by the law of action and reaction. The calculation of contact forces in the NSCD method is performed in two steps. First, the result of the interaction of the antagonist body B_a on the candidate body B_c can be considered equal to the force r_α acting at the contact point of these two bodies. At the contact point, we can define a local frame composed of three vectors (in 3D model) including a normal vector n_α pointing from B_a to B_c and two tangential vectors s_α and t_α, which define the tangential space by respecting this convention $s_\alpha \times t_\alpha = n_\alpha$. On the other hand, we denote g_α the gap distance between bodies along the normal direction. This value will be negative if there is interpenetration between the bodies.

In the second step, one defines a linear mapping H_α that relates the local forces to the global force by the following equation:

$$R_\alpha = H_\alpha(q) r_\alpha \tag{1}$$

where $H_\alpha(q)$ is a mapping which contains the local information about contactors, where q is the configuration parameter which can represent the discretized displacement or any generalized coordinates of the rigid motion. Finally the global contact forces can be obtained by the relation

$$R = \sum_\alpha R_\alpha \tag{2}$$

The same procedure is employed for velocity calculation and the velocity of the bodies can be expressed in the local frame. The relative velocity u_α at the contact point is defined for two bodies in contact by the following equation:

$$u_\alpha = H_\alpha^{\mathrm{T}}(q)\dot{q} \tag{3}$$

where H^{T} is the transpose of H, $\dot{q}$ is the time derivative of q, and t is the time. The relative velocity is decomposed in a normal component represented by $u_{\alpha,n}$ and a tangential component $u_{\alpha,T} = (u_{\alpha,s}, u_{\alpha,t})$.

It should be noted that the derivative of the gap function is equal to

$$t \rightarrow g_\alpha(t) \quad u_\alpha.n\alpha \tag{4}$$

During the evolution of the model with multi-contact systems, shocks may be expected. As a result, these shocks produce velocity discontinuities and make it impossible to define the acceleration as the usual second time derivative of the configuration parameter. Hence, the equation, of motion will be written as

$$M\mathrm{d}\dot{q} = F(t, q, \dot{q})\mathrm{d}t + \mathrm{d}R \tag{5}$$

where $\mathrm{d}t$ is the Lebesgue measure on R, $\mathrm{d}\dot{q}$ is a differential measure denoting the acceleration measure and $\mathrm{d}R$ is a non-negative real measure representing forces and impulses. The matrix M in the Eq. (5) is the mass matrix and the vector $F(t, q, \dot{q})$ collects the internal and external discretized forces acting on the system.

2.2. Frictional contact laws

For determining the value of each component R_α, we need additional information about contact forces. These data are primordial to complete Eq. (5) and also to describe the motion of the system in question.

The impenetrability of contact evoked previously means that it is impossible to have two bodies with crossing boundaries in the system. In addition, it is also considered that the contacting bodies are not attracting each other. In other words, the normal component of the reaction force is always positive or equal to zero when the contact vanishes. This contact behaviour is known as the first unilateral constraint or Signorini condition:

$$g \geqslant 0 \quad r_n \geqslant 0 \quad g.r_n = 0 \tag{6}$$

In the case of cohesive contact, shifting can be applied to r_n and r_t which represents a cohesive force respectively in the normal and tangential directions. This shifting is set to zero if the contact is broken.

The second unilateral constraint, in the case of Coulomb dry friction, can be summarized by the following equations:

$$\begin{cases} \text{if}| \quad \|u_t\| = 0, \quad \|r_t\| \leqslant \mu r_n \\ \text{if}| \quad \|u_t\| \neq 0, \quad \|r_t\| = \mu r_n, \quad u_t = -k r_t, \; k \geqslant 0 \end{cases} \tag{7}$$

The friction force lies in Coulomb's cone ($\|r_t\| \leqslant \mu\, r_n$, μ friction coefficient) and if the sliding velocity is different from zero, friction force is opposed to the sliding velocity with magnitude μr_n.

2.3. Numerical scheme for time integration

One of the most interesting features of the time-stepping integration scheme is included in the fact that it does not have to handle explicitly the contact events, contrary to the usual event-driven scheme. When we proceed to a time discretization on intervals $[t_i, t_{i+1}]$ of length h, our contact problem is solved over the interval in terms of measures of this interval and not in a point wise way. To achieve this property, the Eq. (5) is integrated on each subdivision, which leads to

$$\begin{cases} M(\dot{q}_{i+1} - \dot{q}_i) = \int_{t_i}^{t_{i+1}} F(t, q, \dot{q})\mathrm{d}t + R_{i+1} \\ q_{i+1} = q_i + \int_{t_i}^{t_{i+1}} \dot{q}(t)\mathrm{d}t \end{cases} \tag{8}$$

where the variable $\dot{q}_{i+1}$ denotes the approximation of the right limit of the velocity at the time t_{i+1}, and $q_{i+1} \approx q(t_{i+1})$. For the contact $\mathrm{d}R$, we approximate the measure of the time interval $[t_i, t_{i+1}]$ by $\mathrm{d}R$ denoted by

$$\mathrm{d}R([t_i, t_{i+1}]) = \int_{[t_i, t_{i+1})} \mathrm{d}R \cong R_{i+1} \tag{9}$$

To approximate the two integrals of the system (8), we use a θ-method, which is a first-order scheme using only the configuration parameter and its first derivative. It should be mentioned that a θ-method is an implicit scheme, identical to the backward Euler's scheme when $\theta = 1$. The stability condition of the scheme implies that θ remains between 0.5 and 1. This approximation leads to the following equation:

$$\begin{cases} \int_{t_i}^{t_{i+1}} F(t, q, \dot{q})\mathrm{d}t = h\theta F(t_{i+1}, q_{i+1}, \dot{q}_{i+1}) + h(1-\theta)F(t_i, q_i, \dot{q}_i) \\ q_{i+1} = q_i + h\theta\dot{q}_{i+1} + h(1-\theta)\dot{q}_i \end{cases} \tag{10}$$

To complete the discrete form of the dynamical equation, a discretization of the frictional contact law that is beyond of the scope of this study, must also be performed. A more detailed discussion on the NSCD method can be found in Moreau (1998), Moreau (1988), Jean (1999), Jean et al. (2001), Jean and Moreau (1992), Renouf et al. (2006a), Renouf et al. (2004b).

3. Numerical modelling

A masonry structure is a discontinuous medium consisting of blocks bonded to each other with mortar or without mortar. In addition, this structure has an interface with the surrounding ground. The discrete element method (DEM) is a suitable technique for modelling these structures. By means of the LMGC90 code, the discrete element analysis of a contact–friction model of an arch structure subjected to a seismic event is described here.

The LMGC90® code is based on the NSCD method (Dubois, 2003). Using this code, we analyse the behaviour of an arch whose geometrical characteristics are shown in Fig. 1. The model consists of an arch with 13 rigid blocks and a supporting base that will be subjected to a sinusoidal vibration in three directions. The numbers beside the blocks in these figures represent the order of the blocks in the model, and these numbers will be referred to, in the post-processing section. The blocks in the model are 0.30 m thick and 0.30 m wide, and their density is 2000 kg/m^3.

This simple arch structure will be studied for different mechanical conditions affecting the behaviour of the model at the level of the interface between the blocks, and also between the blocks and the supporting element (Table 1). Therefore, several simulations are performed with the same geometrical configuration, first, with changes of interaction laws, and then, for a given law, with changes of the value of different parameters, in order to perform a sensitivity analysis.

In this study, the contact law used for the cohesive models is the Mohr–Coulomb law: the status at the beginning of calculation is thus a cohesive status. The normal and tangential cohesion thresholds for these models are presented in Table 1. In all cases, the Mohr–Coulomb cone has an aperture half-angle φ. In this study, we also arbitrarily chose to have the ratio $\mathrm{coh}\,t/\mathrm{coh}\,n = \tan(\varphi)$ where $\mathrm{coh}\,t$ is the tangential cohesion threshold and $\mathrm{coh}\,n$ is the normal cohesion threshold. Therefore, for all the cohesive models, this ratio is considered equal to the static friction coefficient 0.7. Once, a cohesive contact is broken, it has a dry friction behaviour with two static and dynamic friction coefficients. More details about cohesive laws used in the NSCD method can be found in Jean et al. (2001).

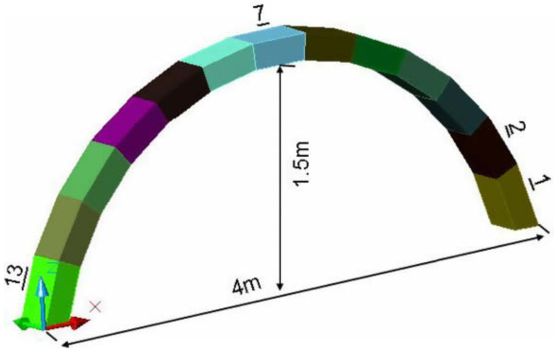

Fig. 1. Geometry of the arch with 13 blocks each 0.3 m wide and 0.3 m thick. The number beside the blocks indicates their order in the model.

Table 1
Interaction contact parameters used for the 10 models, (a) five cohesive models, (b) three dry contact models, (c) two embedded models, with dry contact condition between block (dry friction coefficient 0.7)

		Static friction coefficient	Dynamic friction coefficient	Normal cohesion (Pa)	Tangential cohesion (Pa)
(a) Cohesive models					
1		0.7	0.6	0.1×10^6	0.7×10^5
2		0.7	0.6	0.1×10^5	0.7×10^4
3		0.7	0.6	0.1×10^4	0.7×10^3
4		0.7	0.6	0.1×10^3	0.7×10^2
5	Blocks	0.7	0.6	0.1×10^4	0.7×10^3
	G & B	0.7	0.6	0.1×10^6	0.7×10^5
		Friction coefficient (blocks)			Friction coefficient (G&B)
(b) Dry contact models					
6		0.7			0.9
7		0.7			0.7
8		0.9			0.9
		Static friction coefficient	Dynamic friction coefficient	Normal cohesion (Pa)	Tangential cohesion (Pa)
(c) Embedded models					
9		0.7	0.6	0.1×10^6	0.7×10^5
10		0.7	0.6	0.1×10^4	0.7×10^3

3.1. Sinusoidal oscillations

Regarding the seismic oscillation, hypothetical horizontal and vertical loadings based on a sinusoidal vibration of 2 Hz are applied to the models as velocity functions at the foundation level. We first intend to investigate the behaviour of the structure for a simple sinusoidal vibration before applying a real earthquake loading. In this way, the effects of the different phases of this excitation on the structure can then be distinguished and studied. The sinusoidal excitation is therefore applied in three distinct phases (Fig. 2) including a vertical vibration only during the first second, a horizontal vibration during the second phase, and horizontal and vertical vibrations simultaneously during the last second. The supporting element in the model is given continuous velocities in three dimensions as a function of time. In this way, the arch model is based on an element that acts as a shaking table. The displacement values for the base element are obtained from the post-processing data, recorded during the computation. The horizontal input is applied on both *X* and *Y* directions (Fig. 2).

A three-dimensional modelling of the arch structure, considering stone blocks as rigid elements, is performed with a calculation time step equal to 1 e^{-4} s. The results obtained for the model, with dry friction contacts, are illustrated in Fig. 3 for three different steps. The friction coefficient is 0.7 between the blocks, and 0.9 for the contacts between the lowest blocks and the supporting base element (model 6 in Table 1). As can be seen in these figures, the arch with dry friction contacts has a collapse mechanism similar to a five hinged failure mode. This can be clearly observed in Fig. 3c, and the model seems to conform to Heyman's experimental research on real bridge arches (Heyman, 1982).

Another simulation was performed by taking into account a cohesive law between the blocks with a normal cohesive threshold of 1 KPa, a tangential threshold of 0.7 KPa, a static friction coefficient of 0.7 and a dynamic friction coefficient equal to 0.6 (model 3 in Table 1). It should be noted that this cohesive law changes to the dry friction law once the detachment force between two blocks exceeds the cohesive threshold. For the contact between the blocks and the support element we consider the same cohesive law. The results obtained for this model are similar to those of the first model, but with some differences for the mechanism of collapse. Fig. 4 illustrates the differences between the two models at 2.5 and 3 s of excitation. At 2.5 s, it can be observed that the cohesive model (Fig. 4c) shows more vertical displacement for the central block in comparison with the dry friction model (Fig. 4a), this issue can be clearly seen on the vertical displacement comparative graph for these two models in Fig. 5c. As can be observed in Fig. 4b, in the model with dry friction, the blocks have no resistance against the torsion induced by the sinusoidal vibration. In contrast, Fig. 4d shows the state of the blocks for the cohe-

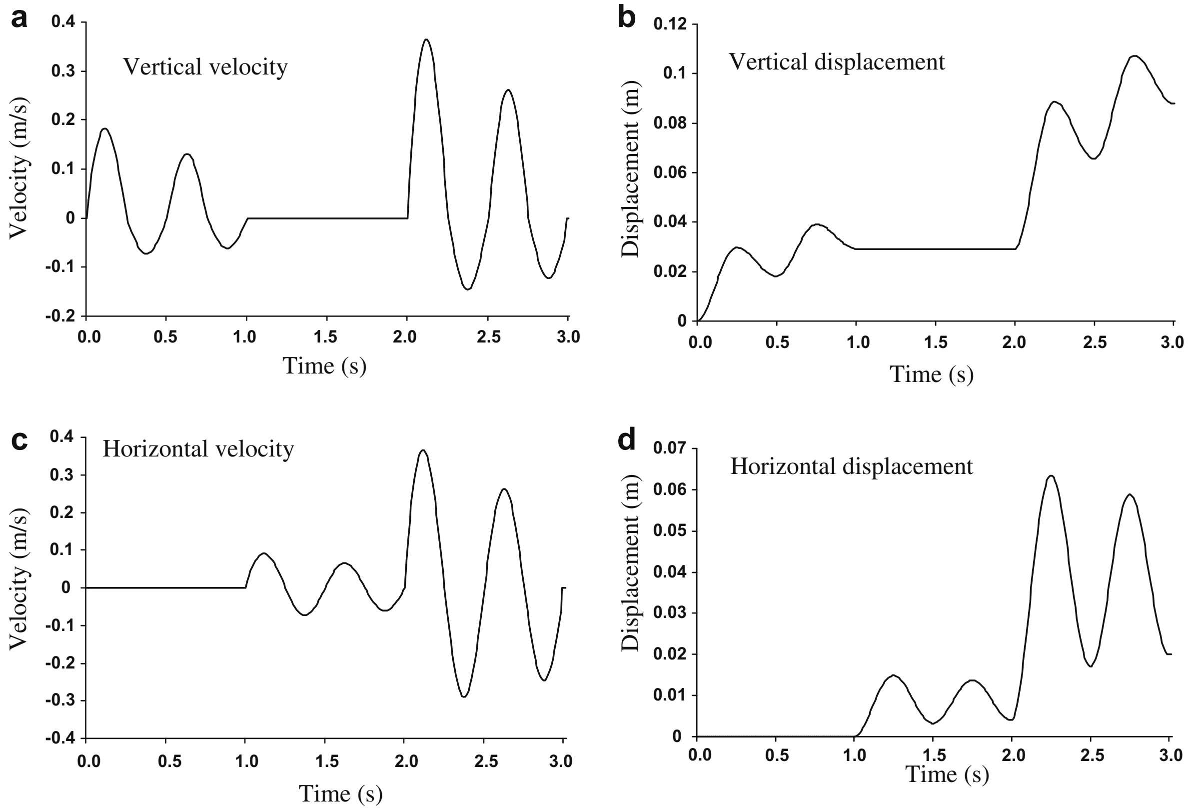

Fig. 2. Time history of input velocity in m/s and displacements caused by these velocities over supporting base element in m. (a) Vertical velocity, (b) vertical displacements, (c) horizontal velocity, and (d) horizontal displacements.

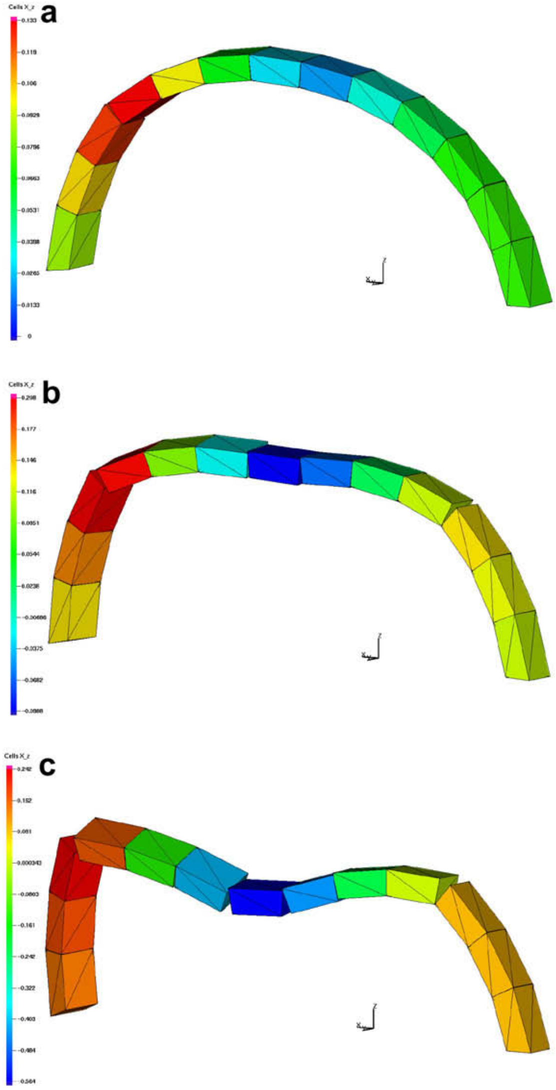

Fig. 3. Collapse mechanism results for vertical displacements (in m) obtained by considering dry friction contact interaction between rigid blocks (model 6 in Table 1b). (a) 2.5 s, (b) 2.8 s, and (c) 3 s (the calculation time step is 1 e^{-4} s).

sive model: the arch in this model does not show any effect of torsion, and the mechanism of collapse happens without any rotation of the blocks, around the axis parallel to the arch.

In addition, a series of simulations was carried out for the models with a strong cohesion between the blocks and the foundation of the model. The results demonstrate that the arch structure remains stable for models 1 and 5 with the cohesive law whose parameters are presented in Table 1. Fig. 5 shows the comparative graphs for the displacement of the 7th block in the model for two simulations including the model with dry friction (model 6 in Table 1) and the model with a cohesive threshold (model 3 in Table 1). As can be seen on these graphs, the central block shows nearly the same behaviour for the vertical displacement for both models, with a larger displacement for the cohesive model around 2.5 s. Regarding the horizontal displacement, the central block shows very different displacements for X and Y directions (Fig. 5a and b). In the case of the cohesive model (model 3 in Table 1), the central block no longer follows the vibration caused by the sinusoidal excitation after 2.5 s, contrary to the dry friction model. The differences in the horizontal displacements between these two models are caused by the last 0.5 s of the sinusoidal vibration: at 2.5 s the direction of the horizontal vibration changes (Fig. 2d).

3.2. *Earthquake excitation*

Since the aim of the paper is the study of the behaviour of this arch structure and its failure modes in the event of seismic motion, in this section, the modelled structure is subjected to a real seismic excitation. The accelerogram of a real earthquake

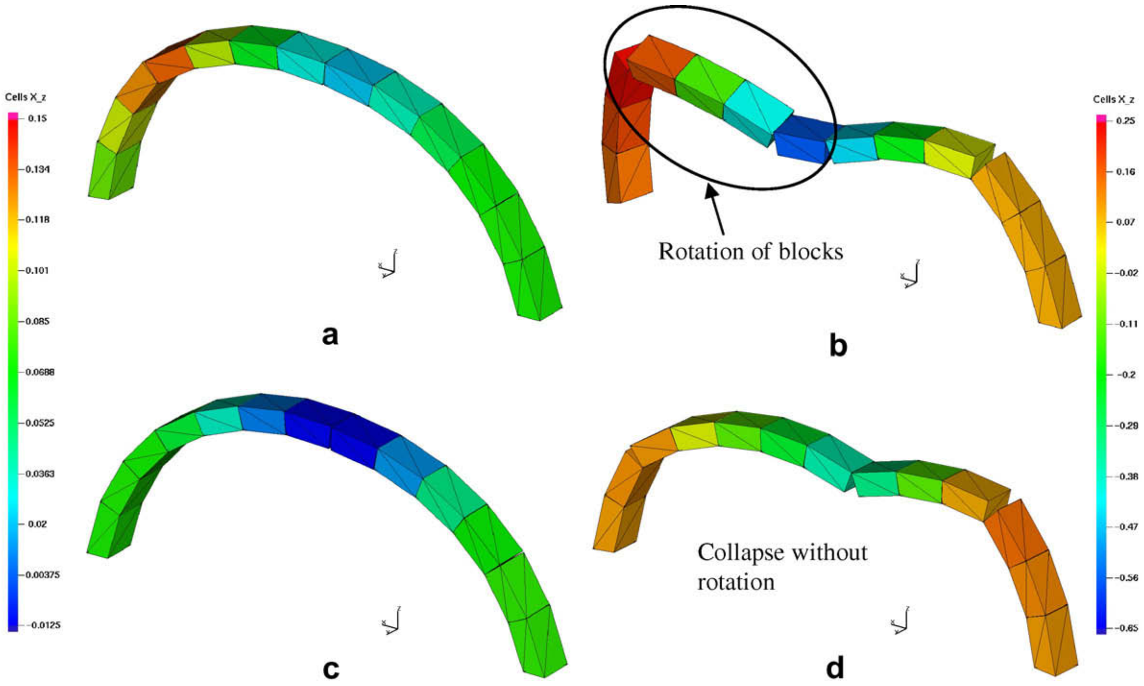

Fig. 4. Collapse mechanism for two models with interaction parameters presented in Table 1. (a,b) Model 6, respectively, at 2.5 and 3 s (c,d) model 3, respectively, at 2.5 and 3 s (the colours represent the displacement in the vertical direction). (For interpretation of color mentioned in this figure the reader is referred to the web version of the article.)

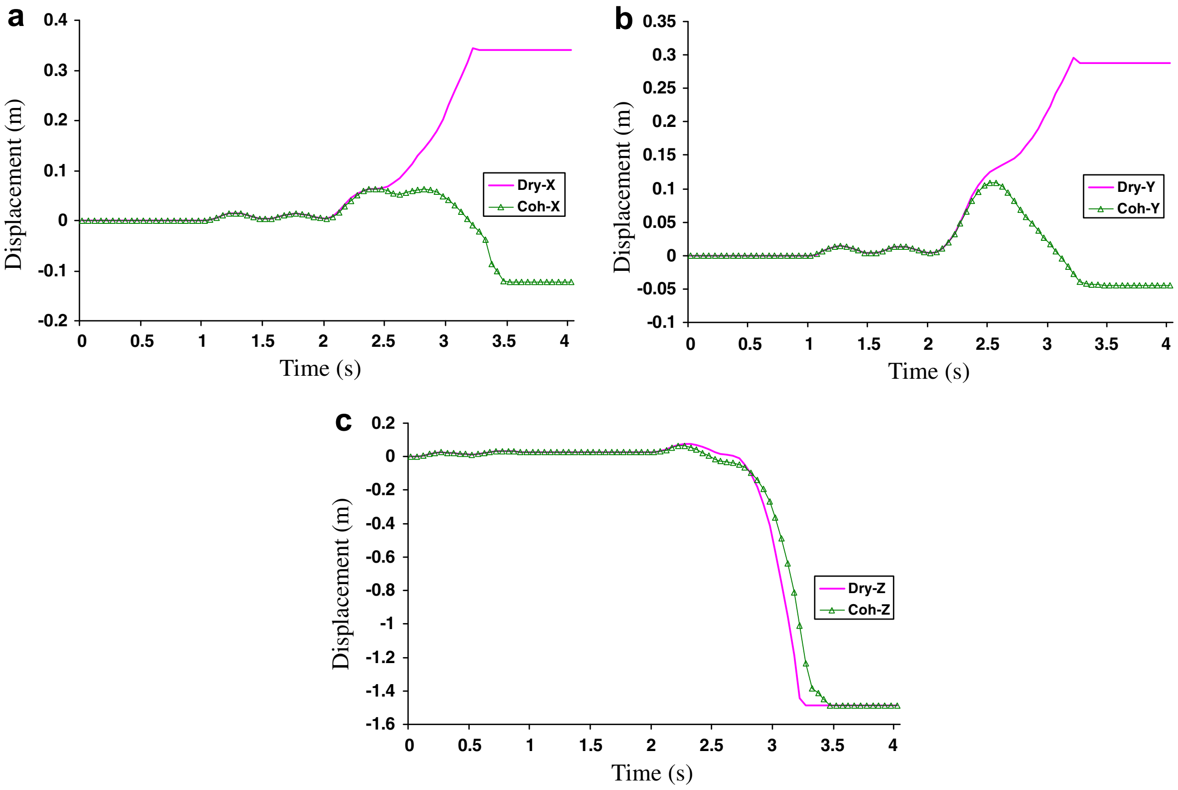

Fig. 5. Displacement variations in meters for both models: cohesive (model 3 in Table 1a) and dry friction (model 6 in Table 1b) versus calculation time for the 7th block indicated in Fig. 1. (a) Displacement in *X* direction, (b) displacement in *Y* direction, and (c) displacement in *Z* direction.

with a maximum vertical acceleration of 0.7 g recorded for 64 s is used in this step (Zanjiran earthquake, Iran, June 20th 1994, an earthquake with an approximate magnitude of 6.1-mb ISMN, 1994). The graphs in Fig. 6 illustrate the recorded accelerations in the three directions and are used to simulate the shaking of the supporting element of the model for the first 15 s. Then a zero velocity is applied in all directions.

These oscillations were applied for all models presented in Table 1 including three categories: cohesive, dry contact and embedded models. Fig. 7 shows the results obtained for five models with cohesive contact condition (Table 1a) at two times: namely 6 and 7 s of the computation time. As it can be seen in these figures, the failure mechanism happens in three cases, but with different characteristics.

With a high cohesive threshold at two levels, block–block contact as well as block–ground contact, the first model remains stable during the 15 s of the seismic excitation. This can be observed on Fig. 8 that illustrates the comparative graph for the vertical displacement of the central block for five cohesive models. The next three models (models 2, 3 and 4 in Table 1a) show instable states for this type of excitation, but each of them behaves differently, especially if we consider the duration of their resistance against the seismic excitation. As anticipated, model 2 resists longer than models 3 and 4. The graph in Fig. 8 illustrates the order of collapse for these three models; the model 4 begins its failure from 5.5 s while the model 2 begins its collapse at 7 s. The mechanisms of collapse observed for these three models are very similar.

The fifth model is a more interesting case, in this model there are two different contact conditions. The cohesive threshold condition used at the level of block–block contacts is weaker than the block–ground contact condition. In this way the effect of a strong embedding over the “weak” structure is investigated. As can be observed in Fig. 7i and j, the model remains stable during the seismic excitation. The graph in Fig. 8 illustrates that this model 5 and model 1 behave in a similar way. Therefore, it can be observed in this type of masonry structure, that the embedding condition plays an extremely important role in the structure stability. Even with weak mechanical characteristics within the structure components, it can resist a strong excitation due to a good embedding condition.

The same procedure is applied for three models with dry contact condition (Table 1b). Fig. 9 shows the results obtained for these models at 5.5 s of the excitation. All these three models show the same mechanism of failure, and none resists during the excitation. The comparative graph for the vertical displacement of the central block (Fig. 9d) illustrates that in all models the central block begins to fall down approximately at 5 s. However, it can be seen that model 6 resists a little longer than the other models. The model 6 (Table 1b) has a higher dry friction coefficient at the level of the embedding. It seems that this model 6 with more flexibility within the structure resist better than model 8.

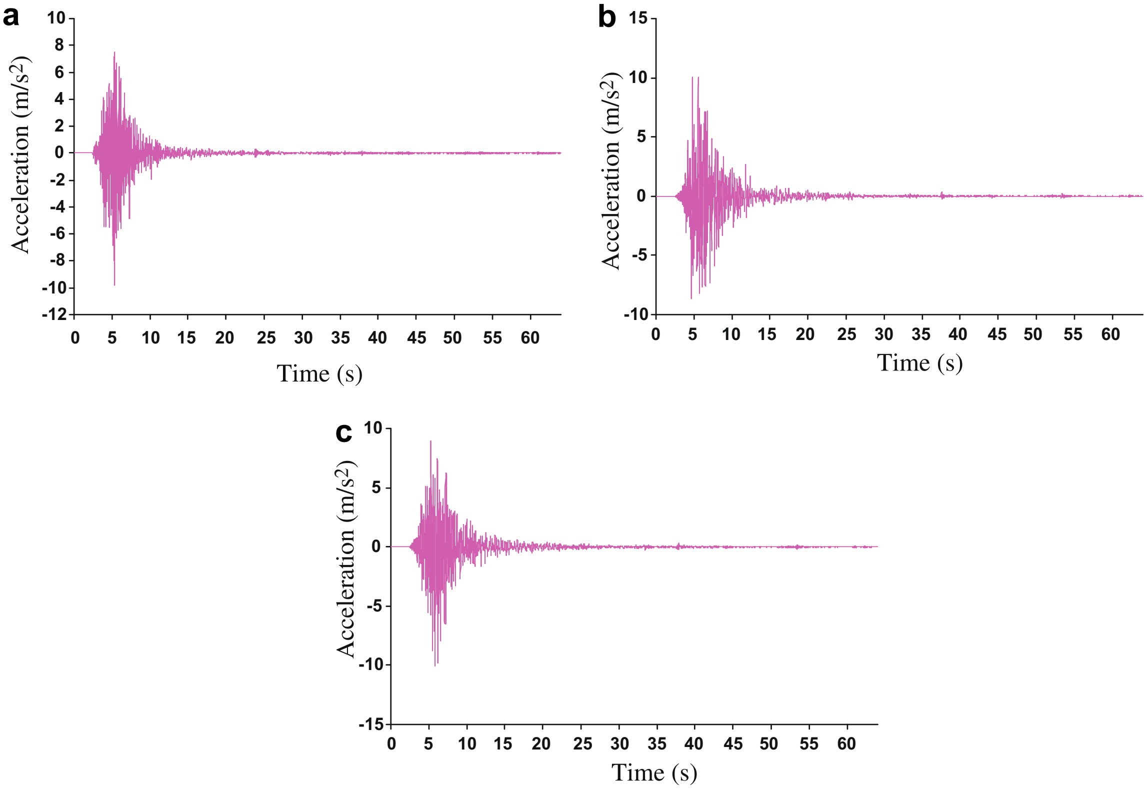

Fig. 6. Accelerogram (a–c) ground acceleration in (m/s^2), respectively, for the vertical, X, and Y directions.

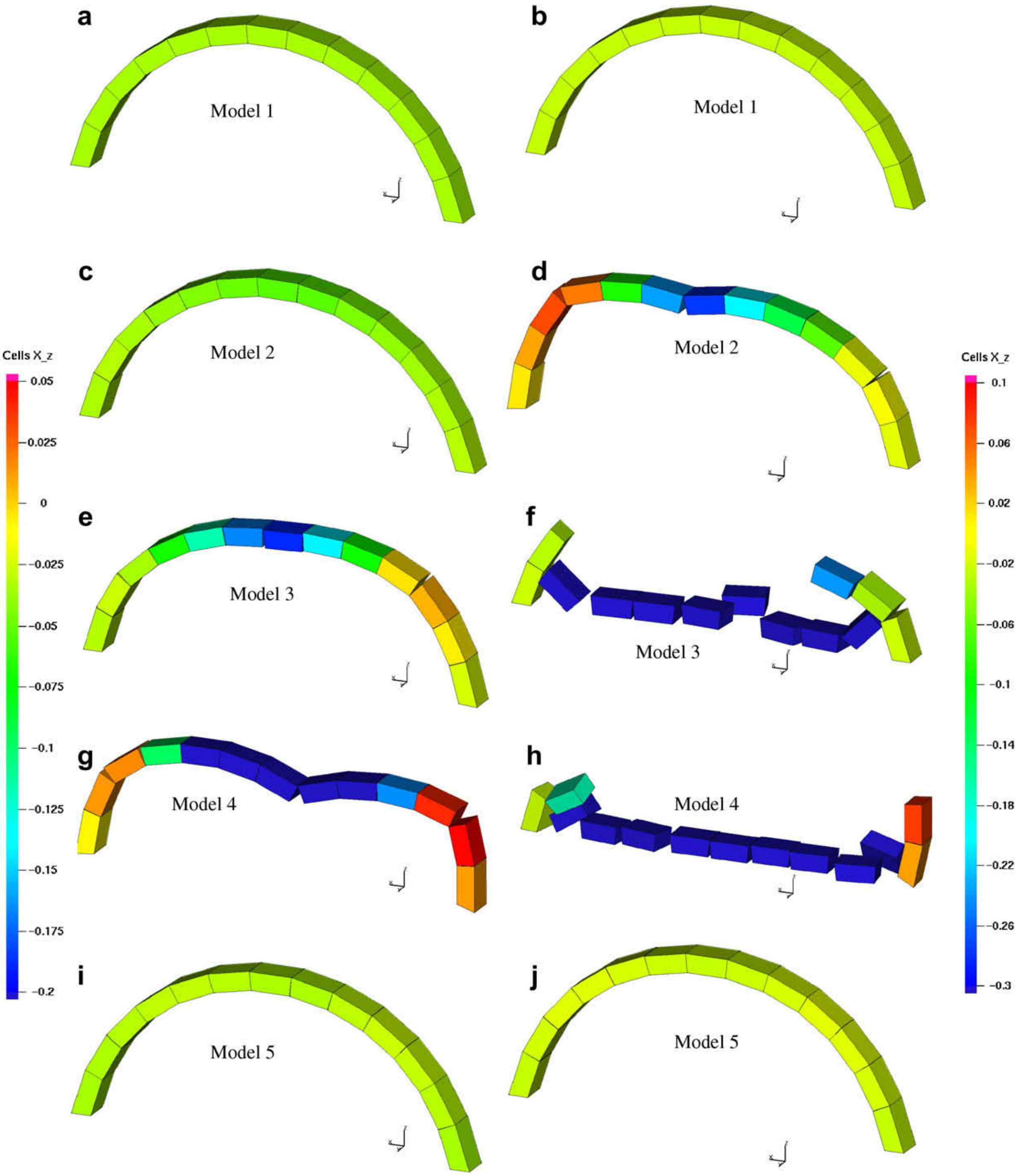

Fig. 7. Collapse mechanism characteristics for five cohesive models (Table 1a) at 6 and 7 s of seismic excitation. (a,b) Model 1; (c,d) model 2; (e,f) model 3; (g,h) model 4; (i,j) model 5 (the colours represent the displacement in the vertical direction). (For interpretation of color mentioned in this figure the reader is referred to the web version of the article.)

The dynamic behaviours of two embedded models (presented in Table 1c) during the seismic excitation are also investigated and compared. Fig. 10 shows the results obtained for these two models. It should be noted that in these models the parameters considered for contact between blocks is dry friction with 0.7 as friction coefficient, and there are cohesive contacts only between blocks 1 and 13 and the ground. The comparison between these two models demonstrates that the model with strong embedding condition, model 9, resists during the seismic excitation, while model 10 with weak cohesion at this level loses its stability. The comparative graph in Fig. 10(e) illustrates the vertical displacement of the central blocks of these two embedded models. It can be observed that model 10 begins to lose its stability at 6 s.

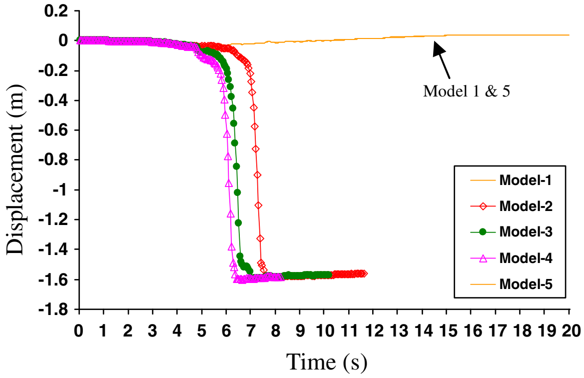

Fig. 8. Vertical displacement variations in meters for the five cohesive models (Table 1(a)) versus calculation time for the 7th block indicated in Fig. 1.

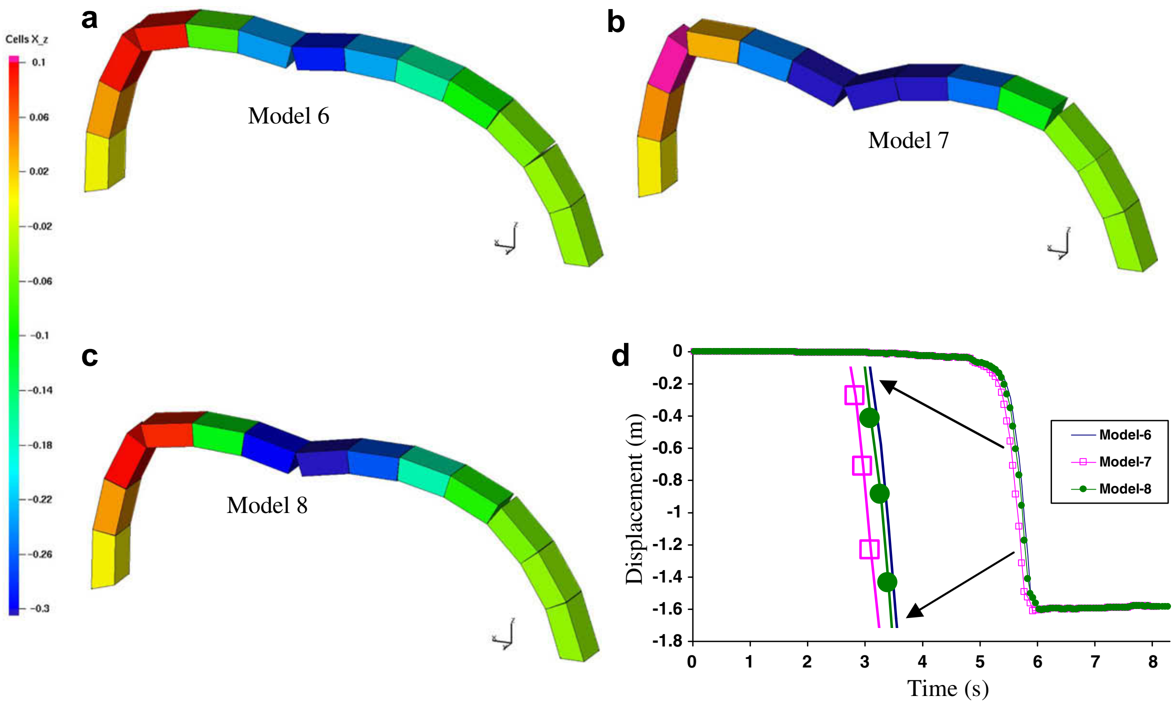

Fig. 9. Collapse mechanism characteristics for three dry contact models at 5.5 second of seismic excitation. (a) Model 6, (b) model 7, (c) model 8 (the contact parameters used for these three models are presented in Table 1(b)), (d) comparative graph for vertical displacement variations in meters versus calculation time for the 7th block indicated in Fig. 1.

In order to compare the maximum horizontal force generated by the seismic excitation on the two blocks in direct contact with the ground, the evolution of the horizontal force before the failure of the arch is examined for the ten models presented in Table 1. Fig. 11a and b shows the evolution of the horizontal force for the 8th model during the first 7 s of calculation, respectively, for blocks 1 ant 13 as indicated in Fig. 1. These two graphs show a sharp increase of the horizontal force around 5.5 s which corresponds to the beginning of the arch failure as illustrated in Fig. 9c. The comparative histogram (Fig. 11c) presents the maximum of horizontal force on the blocks 1 and 13, before the collapse of each model. The differences between the two blocks in the same model can be explained by a possible imbalance of reactions on the two “feet” of the arch, as soon as large relative movements of adjacent blocks happen, in an unsymmetrical way, in the arch. It is interesting to notice that, when the arches remain stable, the two maxima are very similar (models 1, 5 and 9), whereas, when the structure starts to collapse, the maxima on the two blocks are different.

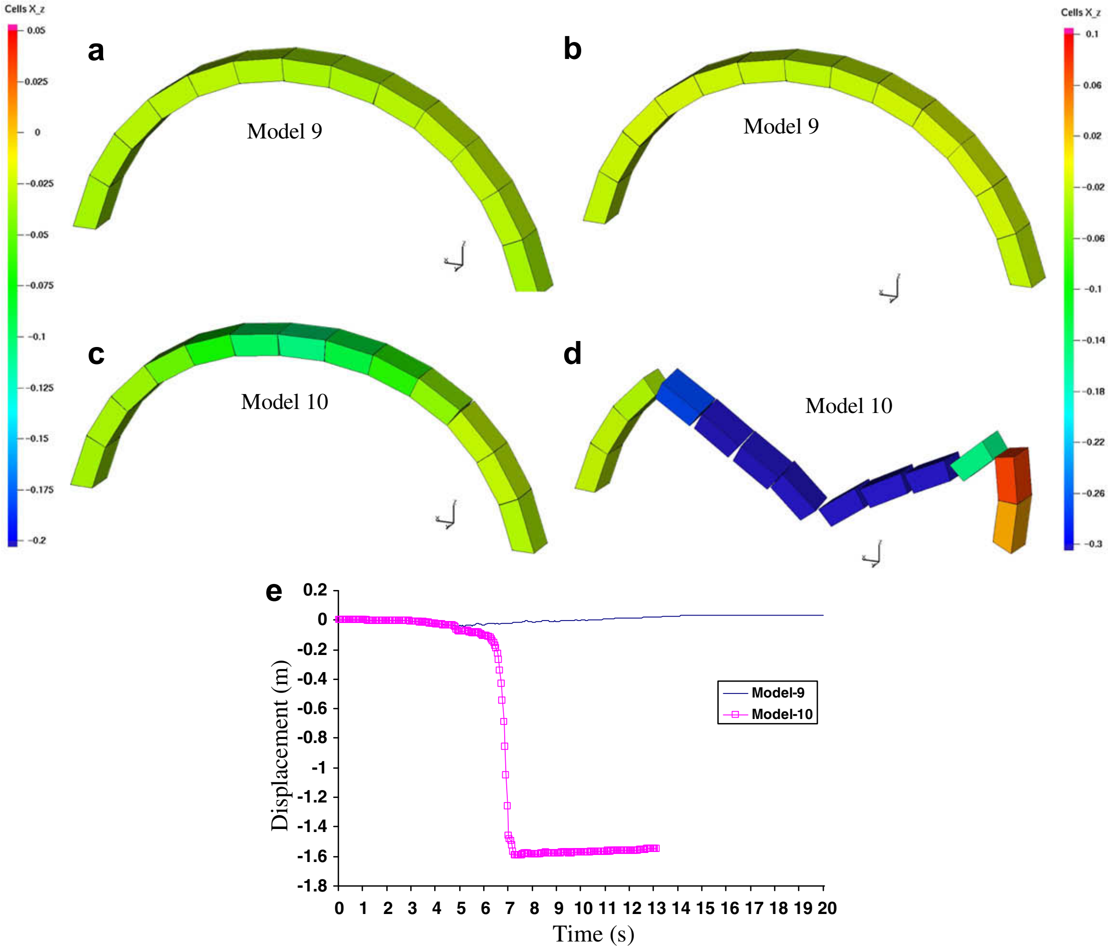

Fig. 10. Collapse mechanism characteristics for two embedded models at 6th and 7th second of seismic excitation (contact condition presented in Table 1(c)). (a,b) Model 9, (c,d) model 10, (e) comparative graph for vertical displacement variations in meters versus calculation time for the 7th block indicated in Fig. 1 for these two embedded models.

4. Arles aqueduct

During the second century AD, the complete rebuilding of an aqueduct bridge at the Vallon des Arcs site near Fontvielle (France) can be explained by the necessity to supply the Roman colony of Arles with water Leveau (1995). The site reveals the presence of two parallel 325 m long aqueducts.

The western bridge was used by the aqueduct leading to Arles, and collected the waters gathered on the north side of the Alpilles Mountains. The second bridge supported a conduit leading to the Barbegal mills. Its water was collected on the south side of the Alpilles. The stone arches have different spans, from approximately 1.5 to 4.8 m, to follow the natural slope of the hill, and the aqueduct consists of 36 piers. The average width of the aqueduct is 2 m (Fig. 12).

The foundations, the piles and the arches are in large assembled dry stone blocks (without mortar), whereas the conduit walls are made of small block masonry. The sealing of the conduit was obtained by a layer of 25 cm of tile concrete and a mortar coating of 5 cm. The large blocks used in the aqueduct construction are shelly yellow limestone, probably extracted from the stone quarry located under the village of Fontvieille (Raffard et al., 1998).

One of the most plausible assumptions is that of a ruin accelerated by consecutive movements of the ground due to the construction of the parallel aqueduct. The addition of stone mass could have involved a compression of the basement layers, up to the limit of their bearing capacity. A seismic phenomenon is not to be excluded either, although the evidence on the site is still missing.

In order to better understand the effect of a seismic excitation on such a structure, a 3D model with real dimensions is studied. In this model, the rigid blocks with a density of 2000 kg/m^3 are used by considering the contact interaction law of dry friction with a friction coefficient of 0.7 between the blocks and of 0.9 between the blocks and the foundation of the structure (model 6 in Table 1b). The same sinusoidal excitation, previously used for the simple arch structure, is also

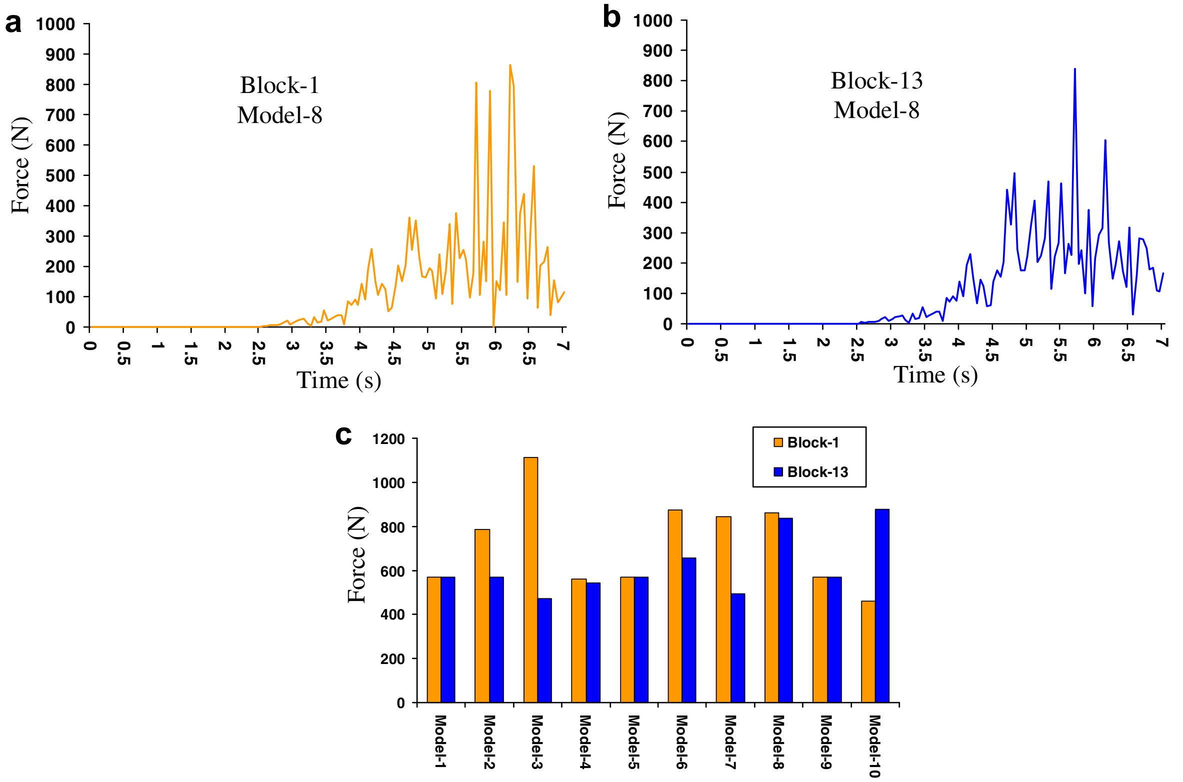

Fig. 11. Horizontal force generated by the seismic excitation during the first 7 s (in N) on the two blocks in direct contact with the ground. (a) Block 1 in the 8th model, (b) block 13 in the 8th model, (c) comparative histogram of the maximum horizontal force for ten models presented in Table 1.

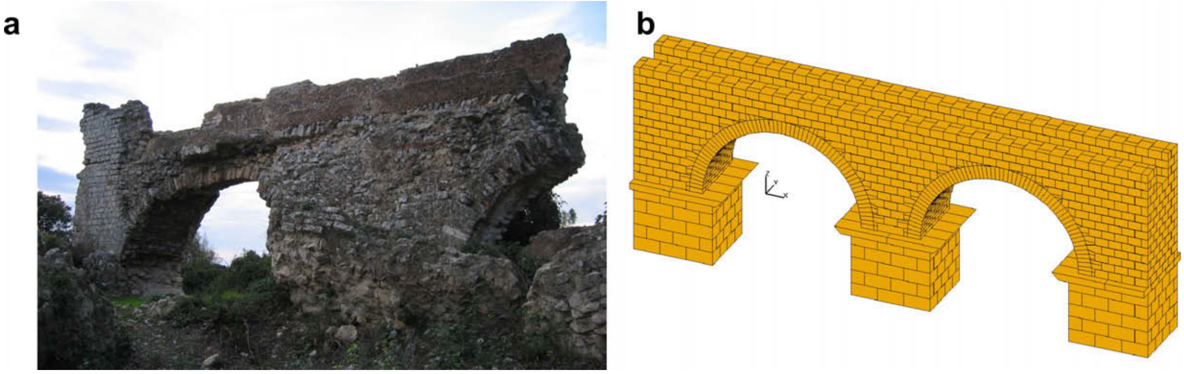

Fig. 12. Arles aqueduct (a) actual state of the structure, with large blocks in the pillars of the arches, and (b) 3D model generated in Auto CAD environment for two arches with 2974 discrete blocks and with an arch span of 4.8 m.

employed to investigate the seismic behaviour of the aqueduct. The horizontal displacements (perpendicular to the aqueduct axis) at the 3rd second, obtained after a 3-s long sinusoidal oscillation (see Fig. 2) are illustrated in the Fig. 13.

Fig. 13a shows the displacements in the *Y* direction, from a lateral perspective view. As can be seen in this figure, a large amount of block displacements is observed in parts of the pillars: this aspect is more obvious in Fig. 13b which displays the structure from above. It should be remembered that the aqueduct width is 2 m. Numerous block detachments in the pillar occur because of the direct contact of these parts of the structure with the support element, directly submitted to the excitation. Therefore, it can be observed in Fig. 13b that there is a relatively high opening between the blocks located in these parts. Fig. 13c shows a close-up view of the arch structure: block detachments are concentred in the outer parts, as can be observed in the *in situ* structure. During the calculation over 50 s, the energy dissipated in the model is recorded and illustrated in Fig. 13d. This graph presents the amount of the energy dissipated by friction and shocks within the model. As can be observed, this energy shows a high increase for the first 3 s, and then remains more or less unchanged.

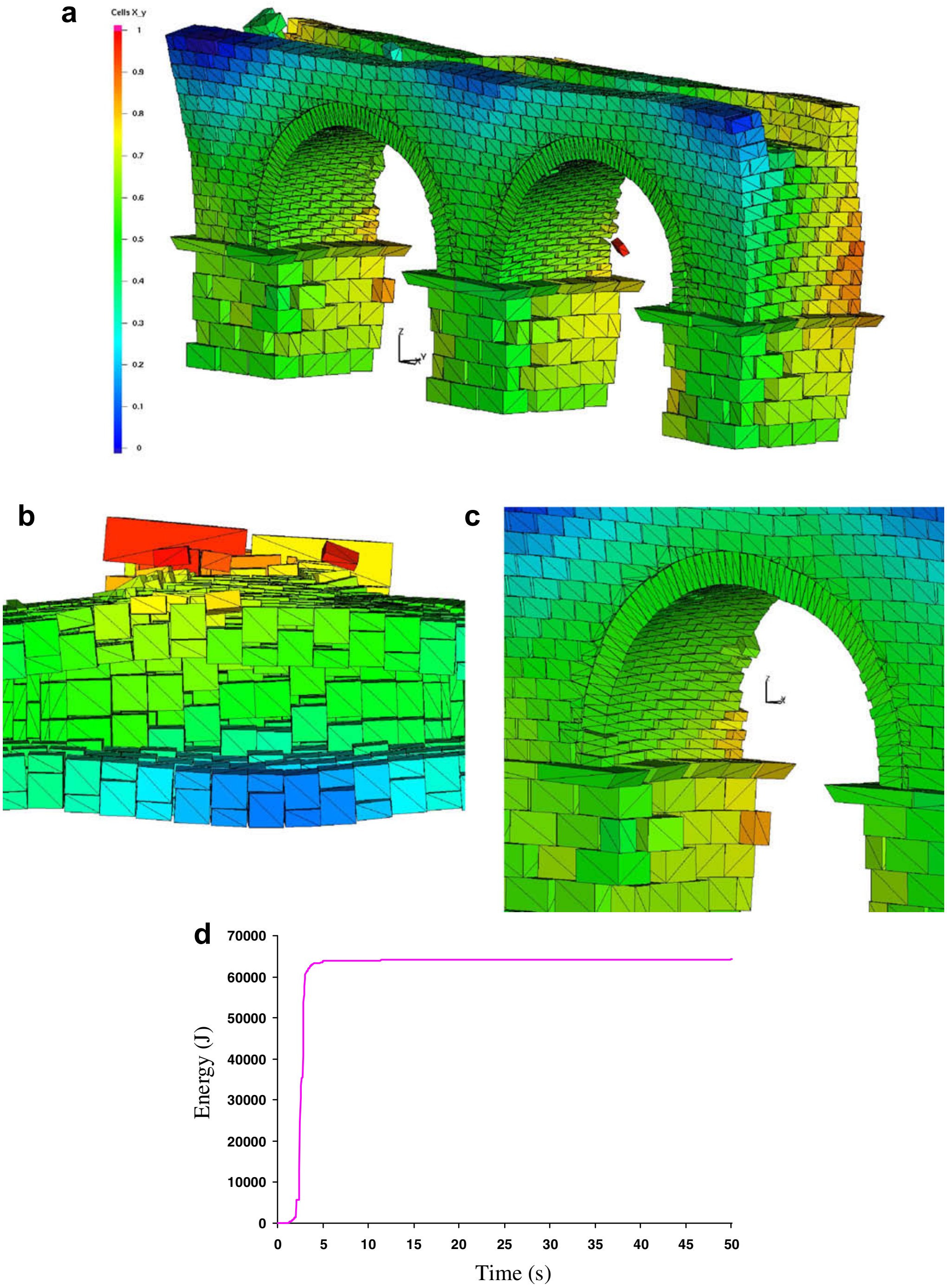

Fig. 13. Displacement distribution in meters for *Y* direction produced by sinusoidal vibrations during 3 s. All pictures show the state of the structure at 3 s. (a) Lateral perspective view of the structure (b) above close-up view of the central pillar (c) close-up view on the left arch of the structure, (d) evolution of the dissipated energy in Joule during 50 s of the calculation.

Finally, in order to better understand the block detachments caused by the seismic vibration, the evolution of the number of contact points versus the calculation time is investigated. The contact point in 3D modelling can be classified in three types: point–face, edge–face and face–face contacts. Therefore, the type of contact can be differentiated by the number of points for each contact. For example, if there are two contact points, it is an edge–face type of contact, and for more than two points, a face–face type is considered. Fig. 14a illustrates the graph of the number of contacts during the 50 s of the

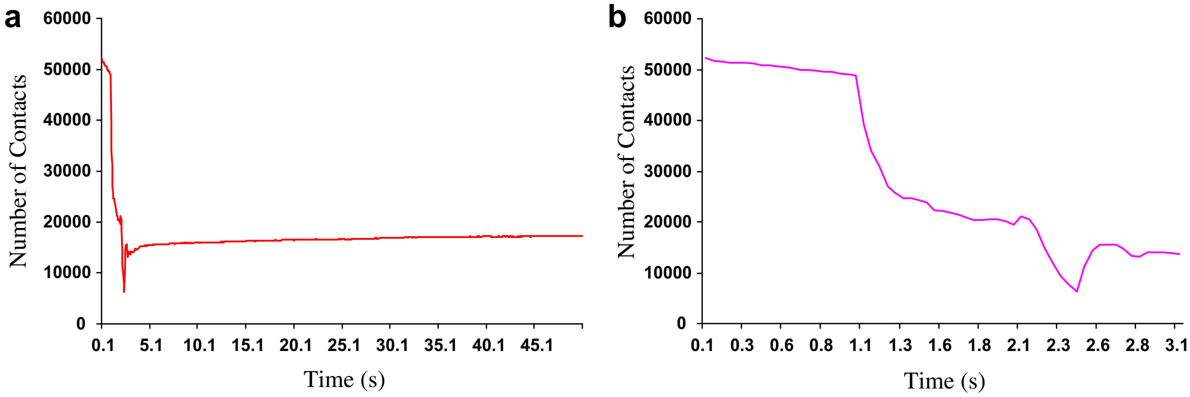

Fig. 14. Evolution of the number of contacts in the model of the Arles aqueduct, subjected to sinusoidal vibrations for 3 s, followed by 47 s of stabilisation. (a) Over 50 s, (b) over the first 3 s.

calculation. As can be observed, the number of contact points before launching the seismic vibration is more than 50,000, but this number drops sharply to less than 10,000 points in the first 3 s (Fig. 14b), i.e., the time during which the model is subjected to seismic excitation. The number of contacts during the first 3 s, (see Fig. 14b) shows two sharp decreases corresponding to changes in the excitation condition (see Fig. 2) after the first and second seconds. This shows a high vulnerability of the masonry structure to such an excitation. The number of contact points then remains around 15,000 until the end of the simulation.

5. Conclusion

In the present study a numerical investigation of a masonry arch subjected to a seismic load has been presented. A unilateral contact friction model is used for the simulation of the arch, with and without mortar. The LMGC90® code is used to model the behaviour of the masonry arch as an assembly of 3D rigid blocks during the seismic excitation. This code is based on the NSCD algorithm that has an implicit algorithm to solve the dynamic equations and it is able to deal with shock events produced within the discrete model during the simulation. One of the advantages of the NSCD method is that there is no need to resort to artificial damping in order to secure its numerical stability (Moreau, 1998).

The seismic vibrations are simulated with the help of sinusoidal oscillations and a recorded accelerogram in the form of the velocity input data that are applied to the base element of the model. The results obtained for several models of the arch with the same geometry but with different contact parameters have been compared. The analysis of the results for the models with dry friction contact indicated that the 3D arch model with rigid blocks conforms to the results obtained for experimental research done on failure mechanisms. The failure mode observed in this numerical case is similar to a five hinges mechanism. Comparisons between the models with the cohesive and the non-cohesive contacts with the foundation show that the arches with cohesive foundations, even those with a weak inner structure, can better resist intensive dynamic excitation.

The behaviour of the historic Arles aqueduct, including several stone arches, subjected to dynamic excitation, was studied. The results obtained demonstrated in real scale the efficiency of the NSCD method for masonry structure simulations, particularly when the structures are subjected to dynamic loads. A high number of block detachments occurred during this short vibration. By considering the observed similarities between the simulated structure and the *in situ* one, it can be concluded that a seismic event could be the reason for the destruction of the Arles aqueduct (circa 150 AD).

References

Acary, V., Blaise, J.Y., Drap, P., et al., 1999. NSCD method applied to mechanical simulation of masonry in historical buildings using MOMA. In: XVII CIPA (International Committee for Architectural Photogrammetry) International Symposium WG3—Simple methods for architectural photogrammetry. Olinda, Brazil.

Bicanic, N., Stirling, C., Pearce, C.J., 1995. Discontinuous modelling of masonry bridges. Comput. Mech. 31, 293–314.

Brookes, C.L., Mullett, P.J., 2004. Services load testing, numerical simulation and strengthening of masonry arch bridges. In: CIMNE. Barcelona, p. 10.

Cundall, P.A., Strack, O.D.L., 1979. A discrete numerical model for granular assemblies. Geo-technique 29, 47–65.

DeJong, M., Lorenzis, L.D., Ochsendorf, J.A., 2007. Numerical modeling of masonry arch stability under impulse base motion. In: ECCOMAS Thematic Conference on Computational Methods in Structural Dynamics and Earthquake Engineering. Rethymno, Crete, Greece.

Drosopoulosa, G.A., Stavroulakisb, G.E., Massalasa, C.V., 2006. Limit analysis of a single span masonry bridge with unilateral frictional contact interfaces. Eng. Struct. 28, 864–1873.

Drosopoulos, G.A., Stavroulakis, G.E., Massalas, C.V., 2006. Influence of the geometry and the abutments movement on the collapse of stone arch bridges. Constr. Build. Mater.. doi:10.1016/j.conbuildmat.2006.09.001.

Drosopoulos, G.A., Stavroulakis, G.E., Massalas, C.V., 2007. FRP reinforcement of stone arch bridges: Unilateral contact models and limit analysis. Composites 38, 144–151.

Dubois, F., 2003. Jean M. LMGC90 une plateforme de développement dédiée à la modélisation des problèmes d'interaction. In: Actes du sixième colloque national en calcul des structures. CSMA-AFM-LMS, pp. 111–118.

Fanning, P.J., Boothby, T.E., 2001. Three-dimensional modelling and full-scale testing of stone arch bridges. Comp. Struc. 79, 2645–2662.

Ford, T.E., Augarde, C.E., Tuxford, S.S., 2003. Modelling masonry arch bridges using commercial finite element software. In: Proceedings of the Nineth International Conference on Civil and Structural Engineering Computing. Netherlands, p. 20.

Gilbert, M., Melbourne, C., 1994. Rigid-block analysis of masonry structures. Struct. Eng. 72, 356–360.

Heyman, J., 1982. The masonry arch. Ellis Horwood Series in Engineering Science. England.

Hofstetter, G., Mang, H., 1995. Computational mechanics of reinforced concrete structures. In: Braunschweig (Germany). Friedr. Vieweg und Sohn Verlag.

Hughes, T.G., Davies, A.W., 1998. The influence of soil and masonry type on the strength of masonry arch bridges. In: Sinopoli, A. (Ed.) Proceedings of Sec., Int. Arch Bridge Conf., pp. 321–330.

Idris, J., Verdel, T., Al-Heib, M., 2007. Numerical modelling and mechanical behaviour analysis of ancient tunnel masonry structures. Tunnel Underg. Space Technol.. doi:10.1016/j.tust.

ISMN, 1994. Zanjiran earthquake, Iran. Available from: http://www.bhrc.ac.ir/ISMN/SHABAKEH/accelerograms/earthquake/ten_years/zanjiran/zanjiran.htm

Jean, M., 1999. The non-smooth contact dynamics method. Comput. Methods Appl. Mech. Eng. 177, 235–257.

Jean, M., Moreau, J.J., 1992. Unilaterality and dry friction in the dynamics of rigid bodies collection. In: Contact Mechanics International Symposium. Lausanne, Switzerland, Presses Polytechniques et Universitaires, pp. 31–48.

Jean, M., Acary, V., Monerie, Y., 2001. Non-smooth contact dynamics approach of cohesive materials. In: Proceedings of the Royal Society (Special Issue on Non-Smooth Mechanics). Phil. Trans. R. Soc. Lond. A 329, 2497–2518.

Jing, L., 2003. A review of techniques, advances and outstanding issues in numerical modelling for rock mechanics and rock engineering. Int. J. Rock Mech. Min. Sci. 40, 283–353.

Leveau, P., 1995. Les moulins de Barbegal, les pont-aqueducs du vallon des Arcs et l'histoire naturelle de la vallée des Baux (Bilan de six ans de fouilles programmées), CRAI, Janvier-mars pp. 115–144.

Melbourne, C., Gilbert, M., 1995. The behaviour of multiring brickwork arch bridges. Struct. Eng. 73, 39–47.

Moreau, J.J., 1988. Unilateral contact and dry friction in finite freedom dynamics. In: J. Moreau, e.P.-D. Panagiotopoulos (Eds.), Non-Smooth Mechanics and Applications. CISM Courses and Lectures. Springer-Verlag, Wien, New York, pp. 1–82.

Moreau, J.J., 1998. Some basics of unilateral dynamics, In: F. Pfeiffler, Ch. Glocker, (Eds.), Unilateral Multibody Contacts, IUTAM Symposium, Munich, Germany. Kluwer academic publishers, pp. 1–14.

Ng, K.-H., Fairfield, C., 2004. Modifying the mechanism method of masonry arch bridge analysis. Constr. Build. Mater. 18, 91–97.

Orduna, A., Lourenço, P.B., 2005. Three-dimensional limit analysis of rigid blocks assemblages. Part I: torsion failure on frictional interfaces and limit analysis formulation. Int. J. Sol. Struc. 42, 5140–5160.

Orduna, A., Lourenço, P.B., 2005. Three-dimensional limit analysis of rigid blocks assemblages. Part II: Load-path following solution procedure and validation. Int. J. Sol. Struc. 42, 5161–5180.

Raffard, D., Vinches, M., Henry, J.P., Leveau, P., Goutouli, M., Thernot, R., 1998. The building of the Roman aqueducts: financial and technological problems. The case of the Arles aqueduct. In: Tenth International Congress on the History of Water Management and Hydraulic Engineering in the Mediterranean Region, In: Gemma C.M. Jansen (Ed.), Cura Aquarum in Sicilia, Syracuse, Italy, pp. 125–133.

Renouf, M., Dubois, F., Alart, P., 2004b. A parallel version of the non-smooth contact dynamics algorithm applied to the simulation of granular media. J. Comput. Appl. Math. 168, 338–375.

Renouf, M., Dubois, F., Alart, P., 2006a. Numerical investigations of fault propagation and forced-fold using a non-smooth discrete element method. Rev. Euro. Method Num. 15, 549–570.

Sumon, S.K., Ricketts, N., 1995. Strengthening of Masonry Arch Bridges. Chapter in Arch Bridges. Publ. Thomas Tellord, London.

Winkler, T., Meguro, K., Yamazaki, F., 1995. Response of rigid body assemblies to dynamic excitation. Earthquake Eng. Struct. Dyn. 24, 1389–1408.